Tuning spin-charge interconversion with quantum confinement in ultrathin Bi/Ge(111) films

C. Zucchetti,[1] M.-T Dau,[2] F. Bottegoni,[1] C. Vergnaud,[2] T. Guillet,[2] A. Marty,[2] C. Beigné,[2] S. Gambarelli,[3] A. Picone,[1] A. Calloni,[1] G. Bussetti,[1] A. Brambilla,[1] L. Duò,[1] F. Ciccacci,[1] P. K. Das,[4] J. Fujii,[4] I. Vobornik,[4] M. Finazzi,[1] and M. Jamet[2,*]

[1] *LNESS-Dipartimento di Fisica, Politecnico di Milano, Piazza Leonardo da Vinci 32, 20133 Milano, Italy*

[2] *Univ. Grenoble Alpes, CEA, CNRS, Grenoble INP (Institute of Engineering Univ. Grenoble Alpes), INAC-Spintec, 38000 Grenoble, France*

[3] *Univ. Grenoble Alpes, CEA, INAC-SYMMES, 38000 Grenoble, France*

[4] *CNR-IOM Laboratorio TASC, 34149 Trieste, Italy*

(Dated: May 4, 2018)

* matthieu.jamet@cea.fr

Spin-charge interconversion (SCI) phenomena have attracted a growing interest in the field of spintronics as means to detect spin currents or manipulate the magnetization of ferromagnets. The key ingredients to exploit these assets are a large conversion efficiency, the scalability down to the nanometer scale and the integrability with opto-electronic and spintronic devices. Here we show that, when an ultrathin Bi film is epitaxially grown on top of a Ge(111) substrate, quantum size effects arising in nanometric Bi islands drastically boost the SCI efficiency, even at room temperature. Using x-ray diffraction (XRD), scanning tunneling microscopy (STM) and spin- and angle-resolved photoemission (S-ARPES) we obtain a clear picture of the film morphology, crystallography and electronic structure. We then exploit the Rashba-Edelstein effect (REE) and inverse Rashba-Edelstein effect (IREE) to directly quantify the SCI efficiency using optical and electrical spin injection.

Bismuth exhibits a series of remarkable electronic properties that have stimulated experimental and theoretical investigations for decades, in particular in electronic transport studies [1–3]. The lattice structure of Bi single layer films resembles that of graphene, while the electronic structure is endowed with a very large spin-orbit coupling of the order of 1.8 eV, which may give origin to topological states [4] or to surface states with a giant Rashba spin-orbit splitting ranging from 0.5 eV [5] to 0.8 eV [6]. Bulk Bi has a rhombohedral crystal structure and is a semimetal with a very small indirect band overlap ($\approx$38 meV), resulting in a low charge carrier density compared with conventional metals. Electrons exhibit a long Fermi wavelength (λ_F) of 40 to 70 nm [7, 8], which is more than one order of magnitude larger than in typical metals. Moreover, the electron effective mass m^* in bismuth amounts to $(0.001-0.26)\,m_e$, depending on the crystalline orientation, with m_e being the free electron mass [9]. The small m^* value combined with the long Fermi wavelength facilitates the observation of quantum size effects (QSE) which can drive semimetal to semiconductor (SMSC) transitions in low dimensional systems [10].

To date, the spin properties of Bi films (spin diffusion length l_{sf} and spin Hall angle θ_{SH}) have shown a large dispersion in experimental values which is probably due to the crystalline state of the material. In amorphous Bi, Emoto *et al.* found: l_{sf}=8 nm and θ_{SH}=0.02 [11] whereas, in polycrystalline Bi films, very different values were obtained: $l_{sf} = 0.11$ nm [12]; 2.1 nm [13]; 16 nm [14]; 20 nm [15] or 50 nm [16] at room temperature up to 70 μm at 2 K

[17] and $\theta_{SHE} = 0.00012$ [15]; 0.008 [18]; 0.016 [14]; 0.019 [16]. Despite the large spin-orbit coupling of Bi, the spin diffusion length is long and the spin-Hall angle ϑ_{SH} quite small, which is detrimental for SCI phenomena or spin-orbit torque switching. For these reasons, much effort has been devoted to the study of Bi-based systems in the ultrathin film limit, where several phenomena were observed such as allotropic transformations [19], the emergence of topologically protected [20] or superconducting [21] surface states and SMSC transition [22], which may give rise to a very rich spin physics.

As a first step to investigate SCI in Bi-based low dimensional systems, we analyze the structural and electronic properties of Bi films as a function of the thickness t. To this purpose, we have grown ultrathin Bi films ($t \approx 0-10$ nm) by molecular beam epitaxy (MBE) on a Bi/Ge($\sqrt{3}\times\sqrt{3}$) $R\,30^\circ$ wetting layer stabilized on a Ge(111) substrate. The Ge substrate exhibits metallic character in the 30-300 K temperature range. In the following, we call the (110)-oriented films the pseudo-cubic (PC) phase and (111)-oriented films the hexagonal phase (HEX) by analogy with the Bi/Si(111) system [19]. Structural characteristics of thin Bi films on Ge(111) were investigated by means of several techniques. The Bi growth proceeds as shown in Fig. 1 by STM: up to $t = 3.5$ nm, we observe the formation of isolated three-dimensional PC flat nanocrystals or nanoplatelets (3D PC phase-Fig. 1 a); for $3.5 < t < 4$ nm, the PC nanocrystals start percolating to form a 2D layer (2D PC phase-Fig. 1 b); for $4 < t < 5$ nm, there is coexistence of the PC and HEX (PC+HEX) phases and above 5 nm we only observe the single crystalline HEX phase (Fig. 1 c). This scenario is compatible with that observed in Ref. 25 and is confirmed by *in-situ* Refection High Energy Electron Diffraction (RHEED) and grazing XRD (see Supplementary Information). The latter technique also shows that both PC and HEX films on Ge(111) exhibit the same bulk Bi lattice parameter.

The electronic properties of *in situ* grown Bi/Ge(111) samples have been characterized by means of ARPES with spin resolution (S-ARPES) at the APE beamline of the ELETTRA synchrotron radiation facility. In Figs. 2 a−e, the ARPES spectra collected along the $\overline{K}-\overline{\Gamma}-\overline{M}$ directions of the Ge(111) surface Brillouin zone (SBZ; sketched in the inset of Fig. 2 a) are reported as a function of the Bi thickness. At the early stages of growth, in the 3D PC regime ($t = 1-3.5$ nm), we observe states crossing the Fermi level (E_{F}) around the $\overline{\Gamma}$ point with a hole character. In analogy with what Bian et al. observed on thin Bi/Si(111)

[26], we conclude that these are surface states with a very short spatial extension of only 2 Bi bilayers (1 BL = 3.28 Å), as shown in Fig. 4 of Ref. 26. In this regime, we do not clearly observe other surface or bulk states close to E_F. For $t = 5$ nm, the band structure has evolved and clearly shows occupied states around $k_{\parallel} = 0.7$ Å^{-1} along both the $\overline{\Gamma}$–$\overline{K}$ and $\overline{\Gamma}$–$\overline{M}$ directions. At this thickness, it is worth comparing our experimental data (Fig. 2 g) with the calculated 2D Fermi surface of Bi(110) (Fig. 2 f) [6, 27]. In the former, we observe a dark ring around $\overline{\Gamma}$ and 12 elongated low-intensity rings centered around $k_{\parallel} = 0.7$ Å^{-1}. This Fermi surface can be reproduced by considering the ARPES results of Agergaard et al. on the (110) surface of bulk Bi [27] and the first principles calculations of Koroteev et al. [6]. Indeed, six equivalent growth orientations of the 2-fold symmetric Bi(110) surface are detected on the 6-fold symmetric Ge(111) surface. The elongated rings correspond to the surface electronic states along the $\overline{M}'$–$\overline{X_1}'$ direction of the Bi(110) SBZ. They are also reported in Fig. 2 d along with the surface hole states at $\overline{M}'$ which cross the Fermi level at $k_{\parallel} = 0.9$ Å^{-1}. Finally, for $t = 9$ nm (Figs. 2 e, h), the band structure is the one of single crystalline bulk Bi(111) [28]. We note here that HEX Bi films grow in registry with Ge(111) (for further details about the crystallography of thin Bi/Ge(111) films, see the Supplementary Information).

The results of S-ARPES are shown in Fig. 3. In Figs. 3 a–d, for $t = 2.5$ nm, we probe the surface states around $\overline{\Gamma}$: they exhibit a counterclockwise helical spin texture with a spin polarization P up to 40%. The spin-momentum locking is due to the strong Rashba spin-orbit coupling in the surface states. In Figs. 3 e–g, we show that the states at $\overline{M}'$ for $t = 5$ nm are also spin polarized ($P \approx 30\%$), but they have a clockwise spin helicity, as predicted by Pascual et al. [29]. The conclusion of this analysis is that both $\overline{\Gamma}$ and $\overline{M}'$ states can participate to SCI, but they would provide opposite contributions, since they are both holes states and have opposite spin helicities.

Based on the accurate knowledge of the atomic and electronic structures of ultrathin Bi films, we then perfomed SCI measurements as a function of the Bi thickness. Charge-to-spin conversion phenomena can be directly probed by exploiting MOKE. In this respect, the detection of an electrically-induced spin accumulation in metals is particularly challenging and it has been limited to low temperature ranges [30]. In our case, we exploit longitudinal MOKE (see Fig. 4 a): an electrical current flows in 1.5 mm-wide Bi/Ge(111) stripes of constant Bi thickness and we detect the Kerr rotation signal coming from the Bi film with

a double modulation technique at room temperature (see Supplementary Information). As shown in Fig. 4 b, up to $t = 3$ nm we detect a large Kerr signal ϑ_k, which results from the electrically-induced spin accumulation in Bi, whereas ϑ_k rapidly decreases as the Bi thickness is increased.

The same qualitative behavior is found when the spin-to-charge conversion generated by a spin current is investigated by either optical spin orientation in Ge [31] or spin pumping from a ferromagnet. Optical spin orientation allows obtaining a spin accumulation with in-plane polarization in Ge by shining circularly polarized light on the sample at a grazing incidence [32]. The spin-polarized electrons then diffuse into the Bi film (Fig. 5 a) [33]. As an alternative to optical spin orientation, we can also inject a spin current by spin pumping from an Al(5 nm)/Co(15 nm)/Al(3 nm) stack grown on top of Bi at the ferromagnetic resonance of the Co layer (Fig. 5 b) [34]. In both cases the spin current generates a transverse charge current, which is detected as a voltage ΔV measured between two electrodes deposited across the Bi film in open circuit conditions. Further details on both techniques can be found in the Methods section and in the Supplementary Information. In Fig. 5 c, we show the results for optical spin orientation measurements: the signal is larger in the 3D PC regime, whereas for $t > 3$ nm, it decreases. Similarly, with spin pumping (Fig. 5 d) at 30 K and 300 K we observe a sharp decrease of the signal above $t = 3$ nm, with no detectable signal for $t > 4$ nm. The signal at 30 K is roughly one order of magnitude larger compared to that at room temperature. To summarize, in all the SCI experiments we observe a conversion signal for $t < 4$ nm, when Bi nanocrystals are present at the surface of Ge(111), whereas the signal is drastically attenuated for the other morphologies.

We can exclude that the Bi/Ge(111)-$(\sqrt{3}\times\sqrt{3})R30°$ wetting layer significantly contributes to SCI since Aruga et al. demonstrated both experimentally and theoretically the absence of spin-polarized states at the Fermi level [35]. Hence, the interconversion takes place within or at the surface of nanocrystals of a given height h and lateral size $a = \sqrt{S}$, being S the nanocrystal area. STM images show that the lateral size a of nanocrystals is comparable to the Fermi wavelength, and since $h \ll a$, quantum confinement effects play a fundamental role in determining the spin-transport properties of the system. Indeed, due to the low effective mass of electrons in bulk Bi, the spacing between discrete energy levels can be large enough to open a bandgap E_g' in Bi nanocrystals [36]. The calculation of E_g' in the Supplementary Informations gives a SMSC transition (i.e., $E_g' \geq 0$) for $a \leq 50$ nm. Hence,

nanocrystals of lateral size $a \leq 50$ nm and thicker than 4 BL (meaning that opposite surface states do not overlap each other [26]) are expected to be semiconducting. From an extensive analysis of STM images (see the Supplementary Information), for $t < 0.9$ nm, the majority of PC nanocrystals are less than 4 BL-thick, the top and bottom surface states overlap and the corresponding SCIs, being of opposite sign, cancel each other. For $0.9 < t < 3$ nm, the nanocrystals satisfy the conditions for a SMSC transition. The surface states do not overlap and are electrically separated because the presence of a bandgap increases the bulk resistance. As a consequence, SCI at each interface is allowed and no communication channel between opposite interfaces is present. We can observe a net SCI signal. This thickness range is reported as a shaded area in Figs. 4 b and 5 c, d, and it nicely fits the thickness range where we experimentally observe a conversion signal. This interpretation is in agreement with the increase of the spin-pumping signal at low temperature. For $0.9 < t < 3$ nm, Bi nanocrystals exhibit a bandgap and the number of thermally excited electrons across this bandgap is lower at 30 K than at room temperature, which increases the bulk resistance. Spin-to-charge conversion takes place at the $\overline{\Gamma}$ states in Figs. 2 a–c due to their helical spin texture shown in Figs. 3 a–d, thus it can be attributed to the IREE. Concerning Kerr measurements, in this thickness range most of the current flows at the Bi/Ge interface, where the conductivity of the Rashba electron gas is large [37]. As a consequence, the REE generates an in-plane spin accumulation, with a spin polarization perpendicular to the current density vector. We detect a very large Kerr signal (Fig. 4 b), which is proportional to the electrically-induced spin density at the Bi/Ge interface, since the absorption length α of the incident light ($\alpha = 16$ nm for $\lambda = 691$ nm) is much larger than the nanocrystal height [38]. Finally, for $t > 3$ nm, nanocrystals exhibit lateral sizes larger than λ_F and start percolating. This reduces and finally suppresses quantum confinement at room temperature. In these conditions, spin-polarized electrons diffuse in the entire film thickness, and being $h < l_{sf}$, the spin-to-charge conversions at both interfaces compensate each other reducing the signal down to zero. Similarly, for charge-to-spin conversion, when nanocrystals become gradually conducting, electrical currents flow at both interfaces, causing opposite spin accumulations, which tend to cancel each other. Hence, the Kerr signal drastically decreases. In a simple model, the effect of quantum confinement on SCI experiments is equivalent to the effect of a variable bulk resistance R_B electrically connecting the top and bottom metallic surface states of resistance R_S. Following Ref. 36, for t <3 nm, quantum confinement leads to

$R_B \gg R_S$ and surface states are electrically insulated from each other. We can observe SCI signals. On the other hand, for t >3 nm, $R_B \approx R_S$ and the charge currents in the top and bottom surface states are shunted through the bulk reducing and cancelling SCI signals. We could not detect any spin-to-charge conversion by spin pumping for $t = 50$ nm. This is indicative of negligible bulk spin-to-charge conversion by inverse spin Hall effect and a long spin diffusion length $l_{sf} > 50$ nm. Starting from $t = 3$ nm, $\overline{M}'$ surface states at E_F develop at the surface of Bi nanocrystals and films as shown in Fig. 2. They exhibit a hole character and a spin chirality opposite to the one of $\overline{\Gamma}$ states (Fig. 3), thus also contributing to the decrease of conversion signals.

Spin-to-charge measurements allow extracting the figure of merit of the conversion occurring at the interfaces (insets of Fig. 5 c,d). It corresponds to the IREE length $\lambda_{IREE} = j_c^{2D}/j_s$, where j_c^{2D} is the 2D charge current density (in A m^{-1}) generated by the 3D spin current density j_s (in A m^{-2}) [23]. The methods to calculate λ_{IREE} from optical spin orientation and spin pumping measurements are detailed in the Supplementary Information: there, we assume that the conversion occurs only in PC nanocrystals that fulfill the conditions $h > 4$ BL (surface states do not overlap) and $a \leq 50$ nm (nanocrystals are semiconducting with high bulk resistance). The fraction of the sample surface corresponding to these nanocrystals is given by the analysis of STM images. In the conversion process, the transverse charge current generated at the nanocrystal interfaces is transfered to the conducting Ge substrate for optical spin orientation experiments and to the Al/Co/Al metallic trilayer for spin pumping experiments. It is then detected as a voltage in open circuit conditions. We obtain a maximum calculated value of ≈ 50 pm by both optical spin orientation and spin pumping for $t \approx 3$ nm. It shows that the spin-to-charge conversion efficiencies are comparable at the Bi/Ge and Bi/Al interfaces and that SCI occurs into the $\overline{\Gamma}$ surface states of Bi regardless the material at the interface. It is important to note that such a calculation is performed under the assumption that the bulk resistance of the nanocrystals is large enough to avoid spin diffusion between the two interfaces. If a lower resistance value were taken into account, the λ_{IREE} value would be drastically larger, so that 50 pm represents a lower bound estimation of the spin-to-charge interconversion efficiency. This λ_{IREE} value is comparable to the ones obtained at different Rashba interfaces such as Ag/Bi (100-300 pm) [23, 39], Ag/Sb (30 pm) [39] or Cu/Bi (9 pm) [12]. For Rashba interfaces, $\lambda_{IREE} = \alpha_R \tau/\hbar$ where α_R is the Rashba coefficient and τ is the momentum relaxation time in the interface states. From Ref. 6, we

can estimate $\alpha_R \approx 1.5 \times 10^{-10}$ eV m at the Bi(110) surface assuming nearly free electrons in surface states, which gives $\tau \approx 0.2$ fs. This value is of the same order of magnitude as τ values obtained at other Rashba interfaces.[12, 23, 40].

To summarize, we carried out careful structural and electronic characterizations of Bi thin films epitaxially grown on Ge(111). SCI in Bi layers was investigated by Kerr effect, optical spin orientation and spin pumping. In all three techniques, a conversion signal was only observed in the $t = 1-3$ nm thickness range corresponding to the presence of Bi(110) nanocrystals. We thus interpreted the results as a consequence of QSE and SCI at the surface of semiconducting nanocrystals by (I)REE. Eventually, we found a λ_{IREE} value as high as 50 pm at the Bi/Ge interface which shows the potential of this interface to manipulate spin currents in Ge. Since this is also the first evidence of SCI triggered by QSE, our results paves the way for the exploitation of QSE to tune SCI, and open a new route to manipulate spin currents in Ge by Rashba effect at the interface with a metal [24].

Acknowledgments

This work was supported by the ANR-16-CE24-0017 project TOP RISE and by the Laboratory of Excellence LANEF of Grenoble (ANR-10-LABX-51-01). The authors would also like to acknowledge Dr. Henri Jaffrès for fruitful discussions.

Author contributions

M.J., F.B., L.D., F.C. and M.F. coordinated the entire project. C.Z. and M.T.D. equally participated to the work. A.P. and A.B. performed STM measurements. M.T.D., S.G., C.V., T.G., A.M., C.B. and M.J. performed XRD and spin pumping measurements, and provided the samples for optical and electrical spin injection. C.Z., F.B., C.V., A.P., A.C., G.B., A.B., M.F., P.K.D., J.F., I.V. and M.J. carried out ARPES and S-ARPES measurements. C.Z. and F.B. carried out MOKE and optical spin injection measurements. C.Z., M.T.D, F.B., A.M., A.P., A.C. and M.J. performed the data analysis. All the authors contributed to the writing of the manuscript.

Methods

Sample preparation. ARPES and STM measurements were performed *in-situ* for bismuth thicknesses ranging from 0 to 10 nm. Bismuth was grown by molecular beam epitaxy on Ge(111) under ultrahigh vacuum (10^{-10} mbar), at room temperature and a deposition rate of 0.5 Å/s. The wetting layer was the

Bi/Ge(111)-($\sqrt{3}\times\sqrt{3}$)$R30°$ surface obtained by depositing 1 ML of bismuth on Ge(111)-(2×2) annealed at 500°C for 10 minutes [25, 41]. 0−10 nm Bi wedges for optical and electrical measurements were grown in the same way. The Bi wedges for optical studies were protected by a ZrO_2(10 nm)/MgO(5 nm) bilayer grown *in-situ*. The first nanometer of MgO was deposited using e-beam evaporation at a very low rate (0.025 Å/s) in order to limit the oxygen pressure in the MBE chamber and avoid partial oxidation of the Bi film. The last 4 nanometers were deposited at a rate of 0.25 Å/s. The ZrO_2 layer is grown *in-situ* by RF sputtering. For spin pumping experiments, we deposited *in-situ* an Al(5 nm)/Co(15 nm)/Al(3 nm) trilayer.

(S-)ARPES measurements. (S-)ARPES measurements were performed using p-polarized synchrotron radiation at the APE beamline of Elettra with a photon energy $h\nu = 50$ eV. The hemispherical electron energy and momentum analyzer (Scienta DA30) is equipped with two very low-energy electron diffraction (V-LEED)-based spin polarimeters. We probe the in-plane components of the spin polarization, and the spin-detection efficiency was corrected using a Sherman function ($S = 0.3$), determined by comparison with the known spin polarization of the Rashba-split surface states measured on the Au(111) surface. The spin polarization P is extracted as: $P = [I^+ - I^-]/[S \times (I^+ + I^-)]$, where $I^{+(-)}$ is the V-LEED scattering intensity measured for the V-LEED target magnetization in the positive (negative) direction. The detailed description of the S-ARPES setup can be found in Ref. 42.

MOKE measurements. Electrically-induced spin accumulation in Bi is detected by means of Longitudinal MOKE (L-MOKE). We used a 691 nm-continuous wave laser as a light source. The s-polarized light was focused on the sample surface with an average polar angle $\vartheta = 45°$, a spotsize of diameter 5 μm and an optical power of $W \approx 125$ μW. The reflected light beam passed through a photo-elastic modulator, which modulated the circular polarization of the light at 50 kHz, and a polarizer, before being collected by a photodiode as described in Ref. 43. We recorded the second harmonic of the signal with a first lock-in amplifier and normalized the result to the sample reflectivity to obtain the pure ellipticity signal. In order to further increase the signal-to-noise ratio, we modulated the charge current at 0.3 Hz and extracted the optical signal with a second lock-in amplifier. Further details are given in the Supplementary Information.

Optical spin orientation. A circularly polarized laser beam ($\lambda = 740$ nm) was focused on the sample with a spotsize diameter $s \approx 1.5$ μm and an optical power $W \approx 19$ mW. Optical spin injection generates a spin-oriented population of electrons in the Ge conduction band, with a spin polarization $P \approx 8\%$ [44]

parallel to the light wavevector inside Ge [32]. Since the experimental geometry is sensitive to the in-plane component of the spin polarization [45], we had the laser beam partially filling off-axis a 0.65 numerical aperture objective, focusing the light on the sample with a polar angle $\vartheta \approx 20°$. The resulting electromotive force is measured under open-circuit conditions. The circular polarization is modulated by a photoelastic modulator at 50 kHz and the signal is demodulated by a lock-in amplifier. Furthermore, to increase the signal-to-noise ratio, we also modulate the light intensity at 21 Hz with a chopper and the signal is extracted by a second lock-in amplifier.

Spin pumping. A transverse radiofrequency field $\mathbf{H}_{\mathrm{rf}}$, generated at the center of a cylindrical X-band resonator cavity ($f = 9.7$ GHz, TE_{011} mode), triggers the ferromagnetic resonance of the Co layer and spin pumping. The charge current is given by $I_{\mathrm{C}} = \Delta V/R$, where R is the resistance measured between the two voltage probes. To remove the Seebeck contribution to the signal at room temperature, we consider: $I_{\mathrm{C}} = (I_{\mathrm{C}}^{+\mathbf{H}_{\mathrm{dc}}} - I_{\mathrm{C}}^{-\mathbf{H}_{\mathrm{dc}}})/2$ where $\mathbf{H}_{\mathrm{dc}}$ is the DC magnetic field applied in the film plane [46].

[1] Fuseya, Y., Ogata, M. & Fukuyama, H. Transport Properties and Diamagnetism of Dirac Electrons in Bismuth. *J. Phys. Soc. Jpn.* **84**, 012001 (2014).

[2] de Haas, W. J. & van Alphen, P. M. *Comm. Phys. Lab. Leiden* **207a**, 3 (1930).

[3] Seebeck, T. J. *Abh. Akad. Wiss. Berlin* **289** (1821).

[4] Aguilera, I., Friedrich, C. & Blügel, S. Electronic phase transitions of bismuth under strain from relativistic self-consistent GW calculations. *Phys. Rev. B* **91**, 125129 (2015).

[5] Ohtsubo, Y. et al., Giant Anisotropy of Spin-Orbit Splitting at the Bismuth Surface. *Phys. Rev. Lett.* **109**, 226404 (2012).

[6] Koroteev, Yu. M. et al. Strong Spin-Orbit Splitting on Bi Surfaces. *Phys. Rev. Lett.* **93**, 046403 (2004).

[7] Garcia, N., Kao, Y. H. & Strongin, M. Galvanomagnetic Studies of Bismuth Films in the Quantum-Size-Effect Region. *Phys. Rev. B* **5**, 2029 (1972).

[8] Duggal, V. P. & Rup, R. Thickness-Dependent Oscillatory Behavior of Resistivity and Hall Coefficient in Thin Single-Crystal Bismuth Films. *J. Appl. Phys.* **40**, 492 (1969).

[9] Lin, Y.-M., Cronin, S. B., Ying, J.-Y., Dresselhaus, M. S. & Heremans, J. P. Transport properties of Bi nanowire arrays. *Appl. Phys. Lett.* **76**, 3944 (2000).

[10] Lin, Y.-M., Sun, X. & Dreseelhaus, M. S. Theoretical investigation of thermoelectric transport properties of cylindrical Bi nanowires. *Phys. Rev. B* **62**, 4610 (2000).

[11] Emoto, H. et al. Conversion of pure spin current to charge current in amorphous bismuth. *J. Appl. Phys.* **115**, 17C507 (2014).

[12] Isasa, M. et al. Origin of inverse Rashba-Edelstein effect detected at the Cu/Bi interface using lateral spin valves. *Phys. Rev. B* **93**, 014420 (2016).

[13] Zhang, H. J. et al. Charge-to-Spin Conversion and Spin Diffusion in Bi/Ag Bilayers Observed by Spin-Polarized Positron Beam. *Phys. Rev. Lett.* **114**, 166602 (2015).

[14] Sangiao, S. et al. Control of the spin to charge conversion using the inverse Rashba-Edelstein effect. *Appl. Phys. Lett.* **106**, 172403 (2015).

[15] Emoto, H. et al. Transport and spin conversion of multicarriers in semimetal bismuth. *Phys. Rev. B* **93**, 174428 (2016).

[16] Hou, D. et al. Interface induced inverse spin Hall effect in bismuth/permalloy bilayer. *Appl. Phys. Lett.* **101**, 042403 (2012).

[17] Lee, K.-I. et al. Electrical spin injection and detection in semimetallic Bi and Bi-Pb films. *Phys. Rev. B* **79**, 195201 (2009).

[18] Fan, J. & Eom, J. Direct electrical observation of spin Hall effect in Bi film. *Appl. Phys. Lett.* **92**, 142101 (2008).

[19] Nagao, T. et al. Nanofilm Allotrope and Phase Transformation of Ultrathin Bi Film on Si(111)-7×7. *Phys. Rev. Lett.* **93**, 105501 (2004).

[20] Ito, S. et al. Proving Nontrivial Topology of Pure Bismuth by Quantum Confinement. *Phys. Rev. Lett.* **117**, 236402 (2016).

[21] Weitzel, B. & Micklitz, H. Superconductivity in granular systems built from well-defined rhombohedral Bi-clusters: Evidence for Bi-surface superconductivity. *Phys. Rev. Lett.* **66**, 385 (1991).

[22] Hoffman, C. A. et al. Semimetal-to-semiconductor transition in bismuth thin films. *Phys. Rev. B* **48**, 11431 (1993).

[23] Rojas-Sanchez, J.-C. et al. Spin-to-charge conversion using Rashba coupling at the interface between non-magnetic materials. *Nat. Comm.* **4**, 2944 (2013).

[24] Oyarzún, S. et al. Evidence for spin-to-charge conversion by Rashba coupling in metallic states at the Fe/Ge(111) interface. *Nat. Comm.* **7**, 13857 (2016).

[25] Hatta, S., Ohtsubo, Y., Miyamoto, S., Okuyama, Y., Aruga, T. Epitaxial growth of Bi thin films on

Ge(111). *Appl. Surf. Sci.* **256**, 1252 (2009).

[26] Bian, G., Miller, T. & Chiang, T.-C. Electronic structure and surface-mediated metastability of Bi films on Si(111)-7×7 studied by angle-resolved photoemission spectroscopy. *Phys. Rev. B* **80**, 245407 (2009).

[27] Agergaard, S. et al. The effect of reduced dimensionality on a semimetal: the electronic structure of the Bi(110) surface. *New J. Phys.* **3**, 15 (2001).

[28] Hirahara, T. et al. Role of Spin-Orbit Coupling and Hybridization Effects in the Electronic Structure of Ultrathin Bi Films. *Phys. Rev. Lett.* **97**, 146803 (2006).

[29] Pascual, J. I. et al. Role of Spin in Quasiparticle Interference. *Phys. Rev. Lett.* **93**, 196802 (2004).

[30] Stamm, C. et al. Magneto-Optical Detection of the Spin Hall Effect in Pt and W Thin Films. *Phys. Rev. Lett.* **119**, 087203 (2017).

[31] Bottegoni, F., Celebrano, M., Bollani, M., Biagioni, P., Isella, G., Ciccacci, F. & Finazzi, M. Spin voltage generation through optical excitation of complementary spin populations. *Nature Mater.* **13**, 790 (2014).

[32] Pierce, D. T. & Meier, F. Photoemission of spin-polarized electrons from GaAs. *Phys. Rev. B* **13**, 5484 (1976).

[33] Isella, G., Bottegoni, F., Ferrari, A., Finazzi, M. & Ciccacci, F. Photon energy dependence of photo-induced inverse spin-Hall effect in Pt/GaAs and Pt/Ge. *App. Phys. Lett* **106**, 232402 (2015).

[34] Ando, K. et al. Inverse spin-Hall effect induced by spin pumping in metallic system. *J. Appl. Phys.* **109**, 103913 (2011).

[35] Aruga, T. et al. Different types of Rashba spin-split surface states on Ge(111). *J. Electron Spectrosc. Relat. Phenom.* **201**, 74 (2015).

[36] Zhang, Z., Sun, X., Dresselhaus, M. S., Ying, J. Y. & Heremans, J. Electronic transport properties of single-crystal bismuth nanowire arrays. *Phys. Rev. B* **61**, 4850 (2000).

[37] Sinova, J., Valenzuela, S. O., Wunderlich, J., Back, C.H. & Jungwirth, T. Spin Hall effects. *Rev. Mod. Phys.* **87**, 1213 (2015).

[38] Hagemann, H.-J., Gudat, W. & Kunz, C. Optical constants from the far infrared to the x-ray region: Mg, Al, Cu, Ag, Au, Bi, C, and Al_2O_3. *J. Opt. Soc. Am.* **65**, 742 (1975).

[39] Zhang, W., Jungfleisch, M. B., Jiang, W., Pearson, J. E. & Hoffmann, A. Spin pumping and inverse Rashba-Edelstein effect in NiFe/Ag/Bi and NiFe/Ag/Sb. *J. Appl. Phys.* **117**, 17C727 (2015).

[40] Shen, K., Vignale, G. & Raimondi, R. Microscopic Theory of the Inverse Edelstein Effect. *Phys. Rev.*

Lett. **112**, 096601 (2014).

[41] Bottegoni, F. et al. Spin polarized surface resonance bands in single layer Bi on Ge(111). *J. Phys.: Condens. Matter* **28**, 195001 (2016).

[42] Bigi, C. et al. Very efficient spin polarization analysis (VESPA): new exchange scattering-based setup for spin-resolved ARPES at APE-NFFA beamline at Elettra. *J. Synchr. Rad.* **24**, 750 (2017).

[43] Yang, Z. J. & Scheinfein, M. R. Combined three-axis surface magneto-optical Kerr effects in the study of surface and ultrathin-film magnetism. *J. App. Phys.* **74**, 11 (1993).

[44] Rioux, J. & Sipe, J. E. Optical injection and control in germanium: Thirty-band k·p theory. *Phys. Rev. B* **81**, 155215 (2010).

[45] Bottegoni, F., Zucchetti, C., Ciccacci, F., Finazzi, M. & Isella, G. Optical generation of pure spin currents at the indirect gap of bulk Si. *Appl. Phys. Lett.* **110**, 042403 (2017).

[46] Shiomi, Y. et al. Spin-Electricity Conversion Induced by Spin Injection into Topological Insulators. *Phys. Rev. Lett.* **113**, 196601 (2014).

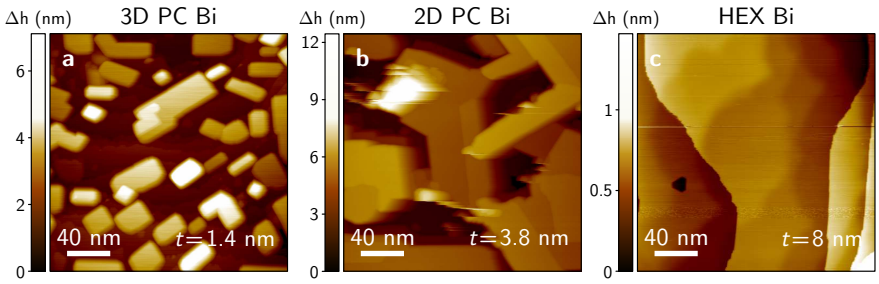

FIG. 1. Morphology of Bi films grown on Ge(111) as a function of the film thickness t**.** Typical STM images of **a**, pseudocubic Bi nanocrystals (3D PC) for $t < 3.5$ nm, **b**, percolated pseudocubic Bi nanocrystals forming a 2D layer (2D PC) for $t = 3.8$ nm and **c**, continuous Bi film with (111)-orientation for $t = 8$ nm. The thickness t is calculated starting from the Bi/Ge(111)-$(\sqrt{3}\times\sqrt{3})\,R\,30^\circ$ wetting layer.

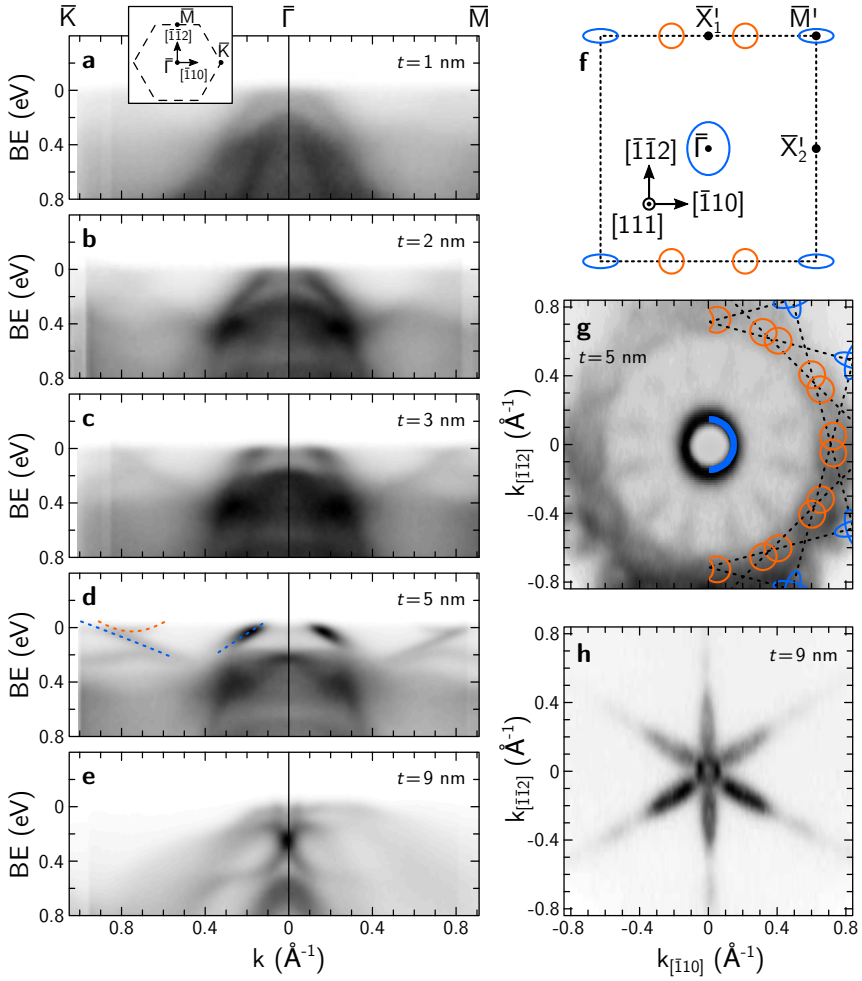

FIG. 2. Thickness evolution of the band structure of Bi/Ge(111) as obtained by ARPES measurements. **a**–**e**, Band structure along the $\overline{K}$–$\overline{\Gamma}$–$\overline{M}$ directions for $t = 1$, 2, 3, 5 and 9 nm of Bi deposited on the Bi/Ge(111)-$(\sqrt{3}\times\sqrt{3})R30°$ wetting layer. $\overline{K}$, $\overline{\Gamma}$ and $\overline{M}$ are high symmetry points of the Ge(111) SBZ shown in the inset of panel **a**. BE and k are the electron binding energy and momentum respectively. Different band structures can be identified depending on the structural phase which are: PC Bi nanocrystals for $t = 1$–3 nm (3D PC phase), a PC Bi film (2D PC phase) for $t = 5$ nm (HEX grains do not give a visible signal) and a (111)-oriented Bi film (HEX phase) for $t = 9$ nm. **f**, Schematics of the Bi(110) 2D Fermi surface according to Ref. 27. $\overline{M}'$, $\overline{\Gamma}' = \overline{\Gamma}$ and $\overline{X_1}'$ and $\overline{X_2}'$ are the high symmetry points of the Bi(110) SBZ. Blue lines (around $\overline{\Gamma}$ and $\overline{M}'$) correspond to hole states while orange ones (near $\overline{X_1}'$) to electron states. They are also reported in **d**. $k_{[\bar{1}10]}$, $k_{[\bar{1}\bar{1}2]}$ and $k_{[111]}$ are the basis vectors of the reciprocal space. **g**, Experimental 2D Fermi surface for $t = 5$ nm reproduced (in orange and blue lines) by superimposing 6 times the Fermi surface of bulk Bi(110) in **f**. **h**, 2D Fermi surface of single crystalline Bi(111) for $t = 9$ nm.

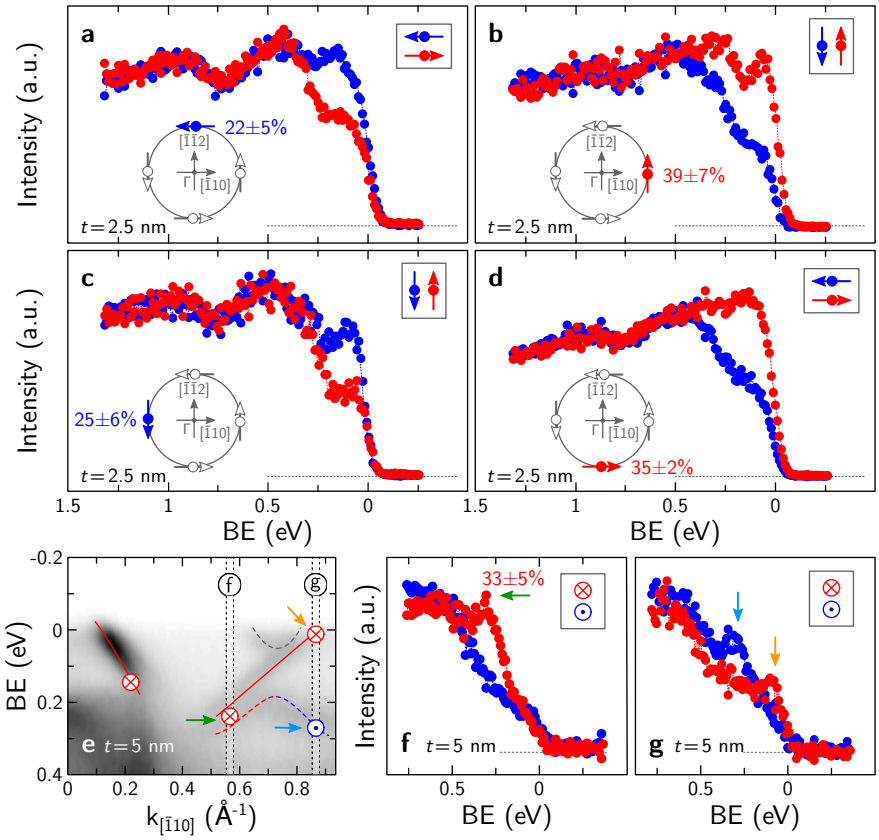

FIG. 3. **Spin-texture of metallic surface states.** **a**−**d**, Spin polarization recorded along the $\overline{\Gamma}$ states showing the helical spin texture, for $t = 2.5$ nm. The numbers are the net spin polarization values. **e**, Band structure along $\overline{\Gamma}$−$\overline{K}$ for $t = 5$ nm. Red solid lines are $\overline{\Gamma}$ ($k_{[\bar{1}10]} \approx 0.1$ Å^{-1}) and $\overline{M}'$ ($k_{[\bar{1}10]} \approx 0.7$ Å^{-1}) hole states of Bi(110) respectively. Dotted lines crossing the Fermi level correspond to the electron pockets near the $\overline{X_1}'$ point shown in Figs. 2 f, g. **f, g**, Spin polarization of $\overline{M}'$ states.

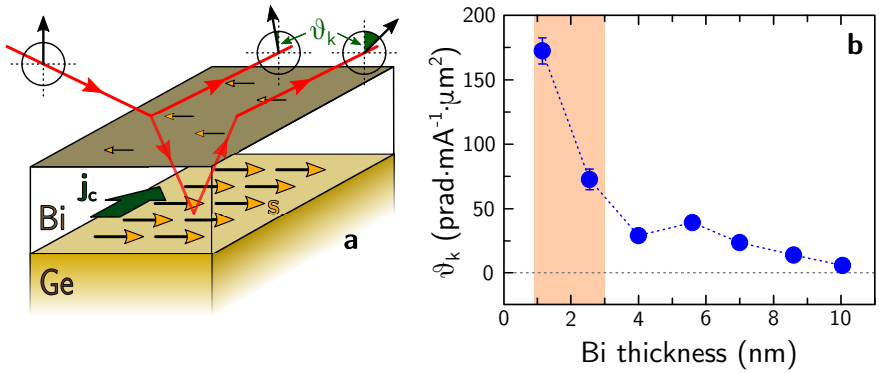

FIG. 4. Charge-to-spin conversion in Bi films probed by MOKE. a, Schematics of the experimental setup for charge-to-spin conversion. An electrical current flows into or at the surface of the Bi layer and is converted into a spin accumulation at the top and bottom surfaces. The spin accumulation at the top surface is detected by longitudinal Kerr effect. **b**, Kerr angle ϑ_k detected as a function of the Bi thickness.

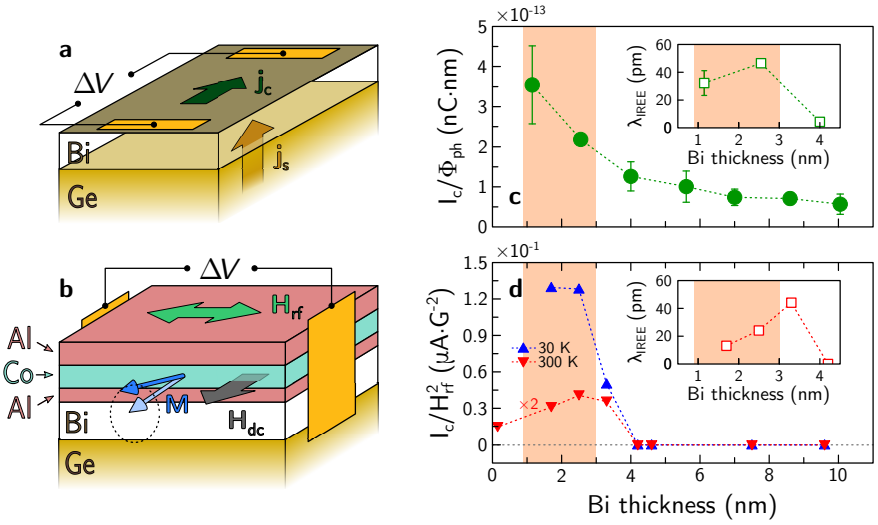

FIG. 5. **Spin-to-charge conversion efficiency probed by either optical or electrical spin injection.** **a, b**, Schematic drawings showing the experimental geometries used for optical spin orientation and spin pumping measurements respectively (for more details refer to the Methods and Supplementary Information). **c**, Bi-thickness dependence of the spin-to-charge conversion efficiency I_C/Φ_{ph} at room temperature using optical spin orientation. $I_C = \Delta V/R$ is the generated charge current where ΔV is the voltage measured in open circuit conditions upon illumination with circularly polarized light and R is the electrical resistance between the two contacts estimated using four-probe resistance geometry. The charge current is normalized to the excitation signal, i.e., the photon flux Φ_{ph}. Inset: λ_{IREE} values deduced at room temperature. **d**, Bi-thickness dependence of the spin-to-charge conversion efficiency I_C/H_{rf}^2 at 30 K and room temperature using spin pumping. $I_C = \Delta V/R$ is the generated charge current where ΔV is the voltage measured in open circuit conditions at the ferromagnetic resonance of the Co electrode and R is the electrical resistance between the two contacts. The charge current is normalized to the excitation signal, i.e., the radiofrequency power proportional to H_{rf}^2. Inset: λ_{IREE} values deduced at room temperature.